A Bistatic Sodar for Precision Wind Profiling in Complex Terrain

STUART BRADLEY

Physics Department, University of Auckland, Auckland, New Zealand

SABINE VON HÜNERBEIN

Acoustics Research Centre, University of Salford, Salford, United Kingdom

TORBEN MIKKELSEN

Wind Energy Division, Risø National Laboratory for Sustainable Energy, Technical University of Denmark, Roskilde, Denmark

(Manuscript received 15 February 2011, in final form 23 April 2012)

ABSTRACT

A new ground-based wind profiling technology—a scanned bistatic sodar—is described. The motivation for this design is to obtain a ''mastlike'' wind vector profile in a single atmospheric column extending from the ground to heights of more than 200 m. The need for this columnar profiling arises from difficulties experienced by all existing lidars and sodars in the presence of nonhorizontally uniform wind fields, such as found generically in complex terrain. Other advantages are described, including improved signal strength from turbulent velocity fluctuations, improved data availability in neutral atmospheric temperature profiles, improved rejection of rain echoes, and improved rejection of echoes from fixed (nonatmospheric) objects. Initial brief field tests indicate that the scattered intensity profile agrees with theoretical expectations, and bistatic sodar winds are consistent with winds from standard mast-mounted instruments.

1. Introduction

In the last few years the use of surface-based remote sensing for wind energy has come to be the preferred method of obtaining wind profiles in the vicinity of large turbines. The useful instruments comprise two types: lidars, which use laser light scattered from naturally occurring atmospheric particulates, and sodars, which use audible sound scattered from atmospheric turbulence (Emeis 2010). Wind components are sensed through the Doppler frequency shift of the light or sound caused by the movement of the target particles or turbulence in the radiated volume above the instrument. Although continuous systems exist, such as the ZephIR lidar from Natural Power (see http://www.naturalpower.com/zephir-300-wind-lidar), nearly all lidars and sodars are pulsed, and the position in the atmosphere from which the scattering occurs is determined by the time of flight of the returning signal. Both the optical and acoustic instruments are faced with the challenge of low received signal levels compared with background noise.

All commercial versions of lidars and sodars are monostatic, meaning that the transmitter and receiver are collocated, and energy from the scattering volume is scattered through 180°. This has the advantage of compactness, and the instruments are more readily deployed in the field because the single instrument package is self-contained. However, Doppler shift from a moving target requires that there be a component of the motion either in the transmitter–target line or in the target–receiver line. This means that to sense three Cartesian coordinate wind components, at least three beams of light or sound have to be transmitted upward and at least two of these must be nonvertical.

For a sound beam transmitted in the direction **T** and scattered energy received from direction **R**, the measured Doppler shift can be written in scaled form as

$$\mu = -\frac{c}{2}\frac{\Delta f}{f_T} = \frac{1}{2}\left(\frac{\mathbf{T}}{|\mathbf{T}|} + \frac{\mathbf{R}}{|\mathbf{R}|}\right) \bullet \mathbf{V}, \qquad (1)$$

where c is the speed of sound, Δf is the Doppler shift, f_T is the frequency of the transmitted sound, and $\mathbf{V} = (u, v, w)$

Corresponding author address: Stuart Bradley, Physics Department, University of Auckland, Private Bag 92019, Auckland, New Zealand. E-mail: s.bradley@auckland.ac.nz

DOI: 10.1175/JTECH-D-11-00035.1

the wind velocity vector (Bradley 2007). In the monostatic case, $\mathbf{T} = \mathbf{R}$ and three measurements would give

$$\mu_b = u_b \sin\theta_b \cos\phi_b + v_b \sin\theta_b \sin\phi_b + w_b \cos\theta_b \quad b = 1,2,3, \tag{2}$$

where θ_b and ϕ_b are the zenith and azimuth angles of the bth beam direction. If $u_b = u$, $v_b = v$, and $w_b = w$ for $b = 1, 2, 3$, then the equations can be solved for the Cartesian wind components u, v, and w.

a. Wind estimation errors in complex terrain

Solving (2) for (u, v, w) requires the assumption of horizontal homogeneity of the wind field, which is probably sufficiently valid above flat terrain but seldom valid over complex terrain. The u components u_1, u_2, and u_3, for example, are in general different because they are the values of the u component in three different volumes. Generally, it is the components directly above the instrument that are required, since this gives "mastlike" wind profiles. Bradley (2008) has developed a potential flow model for estimating remote sensing errors over a bell-shaped hill. The fractional error in estimating the wind speed for a three-beam sodar sited on the crest of the hill, with beam 1 facing downwind, is

$$\frac{\hat{V}}{V_0} - 1 \approx -2\eta^2\frac{z}{H} \approx -5G_{\max}^2\frac{z}{H}, \tag{3}$$

where z is the height of the sensing volume above the hill crest, H is the hill height, η is the ratio of hill height to hill half-width at half-height, and $G_{\max}$ is the maximum gradient of the bell-shaped hill. The fractional error is negative because the maximum speed is directly above the instrument in this case, and the beam directed in the direction of the flow underestimates. So for a hill of maximum gradient 0.1, with $z = H$, a 5% error in wind estimation is predicted. This is comparable to the error measured in practice in complex terrain (Behrens et al. 2012; Bradley et al. 2012) and is unacceptably high for wind energy applications. Note that this error is generic across all sodars and lidars, and is insensitive to the beam zenith angle θ.

Bingol et al. (2009) have proposed a correction method using a flow model (Wasp). However, the reason for doing the in situ remote sensing measurements is because the available flow models are considered insufficiently reliable in complex terrain. This raises the question of whether correcting inaccurate measurements using inaccurate models is a useful approach.

One approach to the distributed sensing volume problem is to expand the wind component variations in the horizontal using Taylor series (Bradley et al. 2012. For example, the u component expands as

$$u(\mathbf{T}) = u(\mathbf{Z}) + [(\mathbf{T} - \mathbf{Z}) \bullet \nabla]u|_{\mathbf{Z}} + \cdots. \tag{4}$$

The correct component above the instrument is $u(\mathbf{Z})$, and the error term contains the vector distance $\mathbf{T} - \mathbf{Z}$ horizontally between the sample volume and the point above the instrument. Note that this expansion *does not* include $\mathbf{R}$. What this means is that, provided the transmission is vertical (i.e., $\mathbf{T} = \mathbf{Z}$), there are no corrections due to horizontal wind shear. But from (1), a monostatic instrument with $\mathbf{T} = \mathbf{Z}$ can only sense $\mathbf{Z} \bullet \mathbf{V} = w$. The main rationale for the work described in this publication is to describe a remote sensing system in which $\mathbf{T} = \mathbf{Z}$ but $\mathbf{R} \neq \mathbf{T}$. Systems in which $\mathbf{R} \neq \mathbf{T}$ are called "bistatic" and necessarily have separated transmitters and receivers, as shown in Fig. 1.

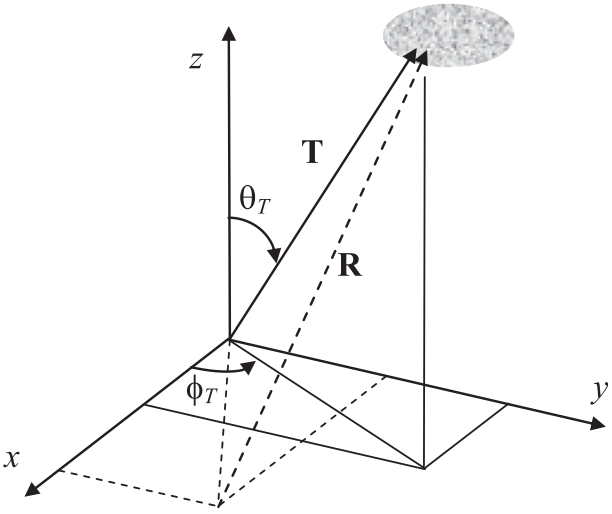

FIG. 1. The bistatic geometry for transmission in direction **T** and reception from direction **R**.

b. Previous bistatic sodar designs

The Doppler shift and scattering cross section for bistatic sodars were analyzed by Thomson and Coulter (1974) and by Wesely (1976). Early experiments with bistatic sodars are described by Coulter and Underwood (1980) and Underwood (1981) for the Risø-78 experiment. For this experiment, there were two bistatic sodars, as shown in Fig. 2. Bistatic system A transmitted at 1 kHz, and system B at 1.6 kHz. Both systems operated in "staring," or nonscanning, mode (the tilted beams had a fixed zenith angle of 60°), but the overlap between the vertical beam and the tilted beams was from about 90- to 200-m height, allowing for profiling over this height range with pulsed transmission. Both systems were pulsed,

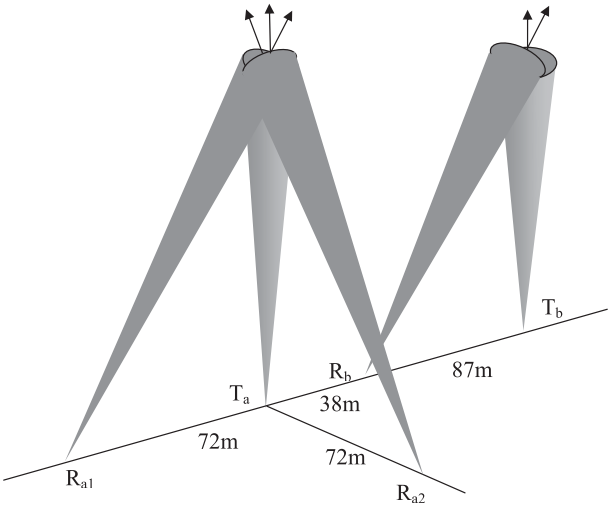

FIG. 2. Dual bistatic geometry of Risø-78.

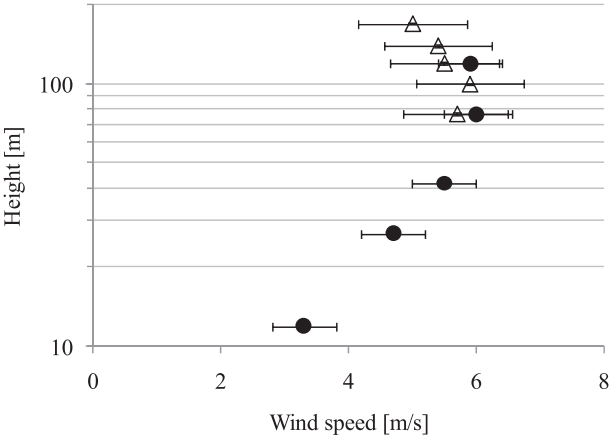

FIG. 3. Comparison between mast (circles) and bistatic sodar measurements (triangles) from the Risø-78 experiment (adapted from Underwood 1981).

defining an instantaneous sensing volume of depth about 17 m. Comparisons with tower measurements 260 m distant are shown in Fig. 3. Although 30-min averages were used, the uncertainties in the bistatic wind measurements are rather large. Values of the structure function parameter for turbulence velocity fluctuations, C_V^2, were also measured at a height of 130 m. The azimuth and elevation angles could be changed manually but this took around 4 min.

Mastrantonio et al. (1986) also presented some preliminary results such as the use of a staring-mode bistatic sodar that could be used simultaneously with a three-axis monostatic sodar, and Mathews et al. (1986) explored refractive acoustic path bending effects for bistatic sodars. Moulsley and Cole (1993) extended the earlier analyses to give a general radar equation for bistatic sodars. Zinichev et al. (1997) described a very large bistatic system having transmitter–receiver separations of 400 m.

Mikkelsen et al. (2007) described ''Heimdall,'' a continuous-transmission staring-mode bistatic sodar design. This operated with vertical transmission at 4 kHz and a single receiver beam of 45° zenith angle at a separation distance of 60 m. The combined temperature structure function parameter C_T^2 and velocity structure function C_V^2 measurements agreed with mast measurements to within an order of magnitude, which is reasonable, given various system uncertainties. It was noted that only 25% of the received scattered energy was expected to be from temperature fluctuations.

Figure 4 shows a spectrum from the Heimdall bistatic sodar. The direct signal from the transmitter to the receiver is obvious in the sharp spectral peak at 3960 Hz. The remainder of the spectral hump comprised two broad bell-shaped spectral peaks. The broader spectral peak to the left is due to the vertically transmitted pulse. Note that it is much broader than the direct signal spectrum because of the wide range of scattering angles for this continuous system. There is also a second broader peak, partly underlying the direct signal peak and slightly to its right. This is due to a diffraction sidelobe from the dish antenna used. Given that $f_T = 3960$ Hz, and the peak at the left is at 3920 Hz (for $\theta = 0$), $u/c = (40/3960)R/D$, where $R = (D^2 + z^2)^{1/2}$ is the distance from receiver to sensing volume and D is the distance from the receiver to the point below the sensing volume. The half-width of the left-hand spectral peak is about 50 Hz, so the range of scattering angles, expressed as $\Delta\theta$, is

$$\Delta\theta = \frac{50}{3960}\frac{1}{\frac{u}{c}\left(1 + \frac{z}{R}\right)} = \frac{50}{3960}\frac{D}{\frac{40}{3960}(R + z)} = 1.25\frac{D}{R + z}. \tag{5}$$

Here $D = z$, so $\Delta\theta = \pm 30°$, which emphasizes the need for bistatic sodars to be pulsed systems. The broad peak at the right, at 3970 Hz, will be from a sidelobe at about 27° from the vertical. Sidelobes at such angles readily exist since they will generally be within the angular pass region of acoustic baffles. For monostatic sodars, such a sidelobe would be unlikely to cause problems, but in the case of this bistatic system it is significant.

In 2010, AQSystem (see http://www.aqs.se/) announced a commercial ''common volume'' configuration comprising three interconnected sodars each having tilted beams that intersect at a common volume in staring mode. A typical configuration is quoted as having all three beams with a zenith angle $\theta = 15°$, the common volume at height $z = 100$ m, and the three sodar units each separated from the point on the ground beneath the sensed volume by a distance of $D = 26$ m. The system is pulsed,

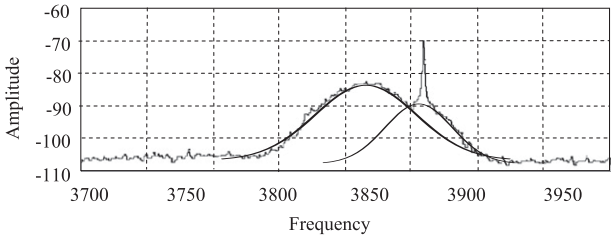

FIG. 4. Heimdall bistatic spectrum (adapted from Mikkelsen et al. 2007).

giving a better definition of the sensed volume. Winds can be obtained only from a single height. Previous bistatic designs discussed above, and the design by Shamanaev (2003), all used fixed-angle antennas, with the limitation of a rather confined height range.

From these examples of previous work it is clear that bistatic sodar systems do give wind profiles, but that (i) they should allow for a nonstaring (i.e., scanned) mode, or a multiple fan-beam staring mode, so as to give a broad height range, and (ii) they should be pulsed so that problems with direct and diffracted beam reception are avoided, and so that the height range of the sensed volume is not so extensive. The design described below accommodates these requirements.

2. Bistatic sodar design principles

Both the Doppler shift and the received amplitude are different for a bistatic system compared with a monostatic sodar. While any configuration of three beams could be used (such as the AQSystem configuration), if the atmosphere is to be scanned in a column, it is more convenient to have one beam pointing vertically since then only two beams need to be scanned. We will concentrate discussion on a single vertical-transmission beam and two tilted receiving beams, with the two planes defined by each tilted beam and the vertical being orthogonal, as in Fig. 5.

a. Signal amplitude

Scattered acoustic power P_R is given by

$$P_R \propto \frac{\sin^2\beta}{(1+\sin\beta)^{11/6}}\frac{e^{-\alpha r}}{r^2}\left[C_T^2 + 3.66(1-\sin\beta)\frac{T^2}{c^2}C_V^2\right], \quad (6)$$

where $r = z + (D^2 + z^2)^{1/2}$ is the total sound path distance, c the speed of sound in air, T is the absolute air temperature, α is the absorption coefficient, C_V^2 and C_T^2 are the turbulent structure function parameters, and $\beta = \tan^{-1}(z/D)$ the elevation angle from the receiver to the sensing volume (Bradley 2007). Bistatic sodars have greater sensitivity than monostatic sodars because of the extra contribution from C_V^2, especially in neutral conditions when C_T^2 vanishes.

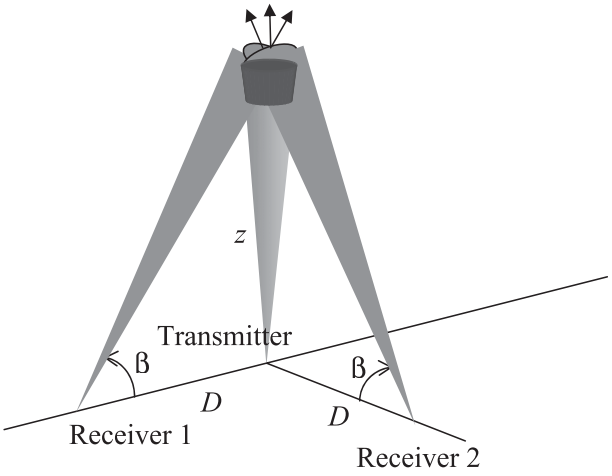

FIG. 5. The geometry of the basic column profiling bistatic sodar.

b. Sensitivity to scattering from rain

Acoustic scattering from raindrops for typical sodar wavelengths is in the Rayleigh regime and has an angular dependence of $(\sin\beta - 2/3)^2$, as discussed by Bradley and Webb (2002). This has a minimum at $\sin\beta = 2/3$ or $\beta = 42°$, whereas from Eq. (6), the scattering from velocity fluctuations peaks at $\beta = 35°$. This means that for much of the bistatic profile, the angular scattering patterns of turbulence and rain favor the scattering from turbulence.

The scattered energy amplitudes from temperature and velocity fluctuations are shown in Fig. 6 for $D = 30$ m and for $D = 50$ m, together with the scattering pattern from rain.

c. Doppler winds

From (1), the bistatic equivalent of (2) is

$$\mu_b = \frac{u}{2}\cos\beta\cos\phi_i + \frac{v}{2}\cos\beta\sin\phi_i + \frac{w}{2}(1+\sin\beta) \quad b = 1,2$$
$$\mu_3 = w, \quad (7)$$

with the solution, for $\phi_1 = \phi_2 - 90° = \phi$,

$$u = [2(\mu_1\cos\phi - \mu_2\sin\phi) - (1+\sin\beta)\mu_3(\cos\phi - \sin\phi)]/\cos\beta$$
$$v = [2(\mu_1\sin\phi + \mu_2\cos\phi) - (1+\sin\beta)\mu_3(\cos\phi + \sin\phi)]/\cos\beta$$
$$w = \mu_3. \quad (8)$$

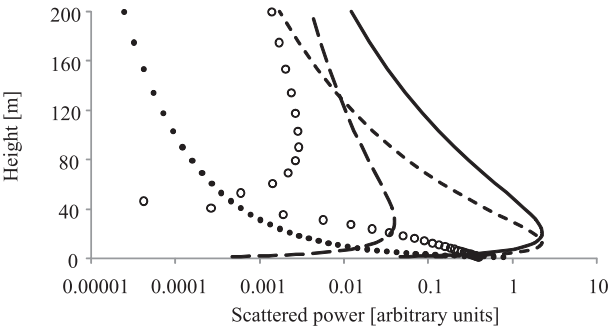

FIG. 6. Relative scattering contributions from turbulent temperature fluctuations (long dashes) and turbulent velocity fluctuations (solid line), vs height, for $D = 50$ m. Also shown (short dashes) is the velocity fluctuation response for $D = 30$ m. The dotted line is the response for a monostatic sodar. Also shown (circles) is the response from rain, with arbitrary scaling.

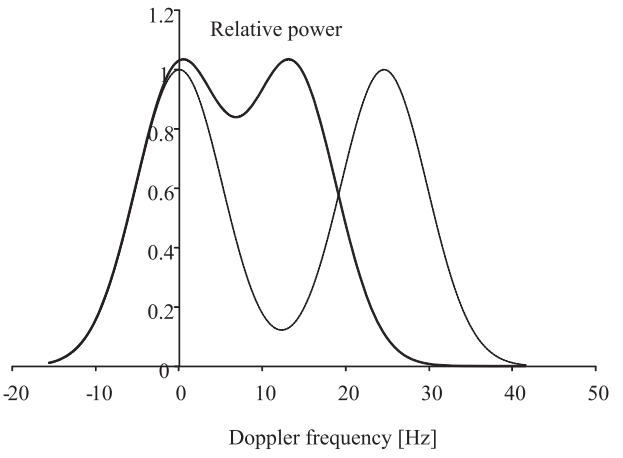

FIG. 7. Sensitivity to spectral corruption due to echoes from fixed objects. Typical sodar parameters are used, as described in the text, and the hard reflecting surface is at a range of 20 m. Combined spectra from the hard surface and the atmosphere are shown for the monostatic case (solid line) and the bistatic case (dotted line).

For example, if $\phi = 0$, the coefficient of u in μ_1, which is proportional to the Doppler shift in beam 1 from the u component, is greater than the corresponding monostatic Doppler shift up to the height of 83 m if the bistatic spacing $D = 50$ m, and the monostatic beam zenith angle is $\theta = 15°$.

The Doppler contribution from w in beams 1 and 2 is always larger than the monostatic case. This increased Doppler helps discriminate against echoes from fixed objects around the sodar. For example, assume a hard reflecting surface is at a range of 20 m and the atmospheric scattered signal is of the same amplitude as that from the fixed surface. For a horizontal wind speed component of 2 m s^{-1} in the plane of a beam and with a pulse duration of 0.1 s, a transmitted frequency of 4500 Hz, a monostatic beam zenith angle of 15°, and a bistatic baseline of $D = 50$ m, Fig. 7 shows the corresponding Doppler spectra for a monostatic sodar and a bistatic sodar. The much improved resolving power of the bistatic system is evident.

d. Scanning geometry

Sodars normally have a pulse duration of about $\tau = 0.1$ s, corresponding to a height resolution of $\Delta z = c\tau/2 = 17$ m. In the case of a scanning, pulsed, bistatic design, the pulse height will define the sensing volume height, but for maximum signal gain the beamwidth of the scanned beam should not be so large that much of the sensitive beam area is outside the pulsed volume. The antenna for typical sodars has a diameter L of between 0.5 and 1.0 m, and the width of the sodar beam, from peak to the first null, is about

$$\Delta\beta = \frac{2\pi}{kL} = \frac{c}{Lf_T}, \tag{9}$$

where k is the acoustic wavenumber and f_T is the transmitted frequency. For $f_T = 4500$ Hz, $\Delta\beta = 2.7°$ for $L = 0.8$ m. At 80-m height, for example, the diameter of this beam would be about 15 m, or close to the typical height extent defined by the pulse duration. Figure 8 shows schematically how the sampling volume is defined by the product of three Gaussian spatial functions: one for the transmitted beam, one for the received beam, and one for the transmitted pulse.

For example, if $f_T = 4500$ Hz, $L = 0.8$ m, $D = 50$ m, and a Gaussian pulse is used having a temporal standard deviation of 0.02 s; the sampling volumes at 30, 50, and 80 m are as shown in Fig. 9.

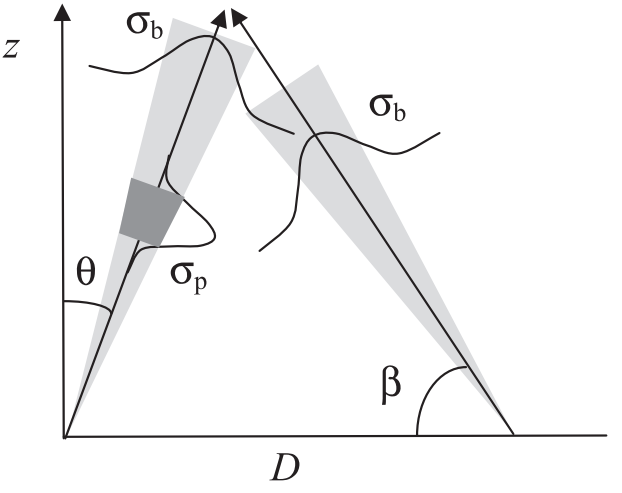

FIG. 8. The three Gaussian spatial functions defining the bistatic sampling volume.

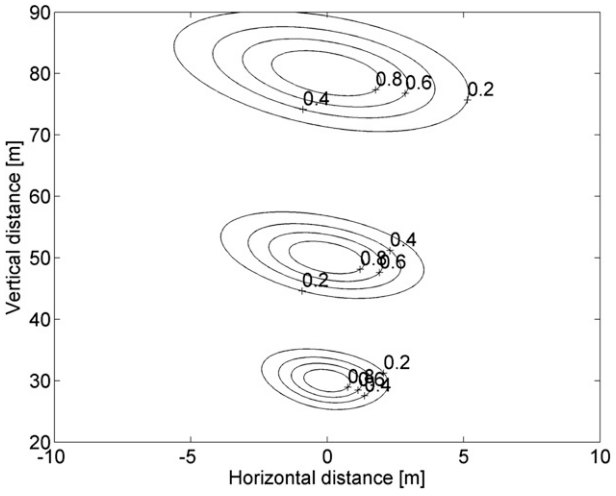

FIG. 9. Sampling volume sensitivity, relative to 1 at the center, for pointing heights of 30, 50, and 80 m. Parameters are $f_T = 4500$ Hz, $L = 0.8$ m, $D = 50$ m, and pulse sigma = 0.02 s.

Given the above, a reasonable design starting point is to have the scanned receiving arrays about 1 m in length. For a prototype bistatic receiver, we have used Motorola KSN1005A superhorn tweeters as microphones. These have a diameter of $d = 0.085$ m and, because our multichannel dataloggers have 12 channels, we used $M = 12$ of these microphones in a linear array, giving a length $L = 0.935$ m. To limit the lateral extent of the sensitivity, we used a 12×3 array, with each row of three microphones connected in parallel to a low-noise preamplifier. This gave a lateral half-beamwidth of 12.7°.

The pointing direction of each microphone array is controlled by adding a progressive phase shift $\Delta\varphi$ to each row down the length of the linear array of microphones (Bradley 2007). To obtain the best sensitivity, each array is mounted on a tripod and aimed at a height z_0, at an elevation angle of β_0.

The pointing elevation angle, β_g to the center of a range gate sampling volume at height z_g, is

$$\beta_g = \beta_0 + \sin^{-1}\frac{\Delta\varphi}{kd} \quad \text{and} \tag{10}$$

$$\frac{\Delta\varphi}{kd} = \frac{D}{(D^2 + z_0^2)^{1/2}}\frac{z_g - z_0}{(D^2 + z_g^2)^{1/2}}. \tag{11}$$

e. Scanning implementation

The voltage output $s_m(t_i)$ from microphone m ($m = 1, 2, \ldots, M$) is recorded at times $t_i = i\Delta t$ ($i = 1, 2, \ldots, N$), with time $t = 0$ being the start of the transmission of the acoustic pulse. The first scattered sound from the air just above the transmitter arrives at the receiver array at time $t_0 = D/c$. Signals from a range gate at height $z_g \pm \Delta z_g/2$ arrive between time $\{(z_g - \Delta z_g/2) + [D^2 + (z_g - \Delta z_g/2)^2]^{1/2}\}/c$ and $\{(z_g + \Delta z_g/2) + [D^2 + (z_g + \Delta z_g/2)^2]^{1/2}\}/c$ or, say, $i = i_g, i_g + 1, \ldots, i_g + (N_g - 1)$. Within this time period, the phased array receiver needs to be staring at this sensing volume, which is achieved by applying the correct incremental phase shift across the array microphone elements.

TABLE 1. Typical parameters for $f_s = 12$ kHz, $D = 50$ m, $z_0 = 60$ m, and a design vertical resolution of 20 m.

z_g (m)	Δt_g (μs)	i_g	Δu (m s^{-1})
20	−125	353	1.0
50	−21	1412	1.4
80	30	2471	2.0
110	58	3529	2.6
140	74	4588	3.3
170	85	5647	3.9
200	92	6706	4.6
160	82	5294	3.7
180	88	6000	4.1
200	92	6706	4.6

All of this processing can be done *after* recording the whole time series $s_m(t_i)$. Delays of any precision can be applied through Fourier transforms:

$$\begin{aligned} S'_{mg}(f) &= \int_{t_{i_g}}^{t_{i_g}+(N_g-1)} s_m(t - m\Delta t_g)e^{j2\pi ft}\,dt \\ &= (e^{jm(f/f_T)\Delta\varphi_g})\int_{t_{i_g}+m\Delta t_g}^{t_{i_g}+(N_g-1)+m\Delta t_g} s_m(t^*)e^{j2\pi ft^*}\,dt^* \\ &= P_{mg}(f)S_{mg}(f), \end{aligned} \tag{12}$$

where $\Delta t_g = \Delta\varphi_g/(2\pi f_T)$. We select the Δt_g by selecting the range gate limits. This in turn determines N_g. For a sampling frequency $f_s = 1/\Delta t = 12$ kHz, and $\Delta z_g = 30$ m, we get $N_g = 1059$ and the other range gate parameters shown in Table 1. The time delays are small compared with Δt, emphasizing the need (at lower sampling frequencies) for using Fourier delays rather than indexing into the time series table. Note that the beam steering time delays are so small that they do not need to be accounted for in the Fourier integral (or indexing for each spectrum). The last column in Table 1 contains the velocity increment corresponding to the frequency increment in the Fourier transform. Once these parameters are determined, the M Fourier transforms $S_{mg}(f_i)$ are found for this range gate. Each complex spectral component from S_{mg} is then multiplied by the complex number $P_{mg}(f_i)$ to form the complex spectrum S'_{mg}. Finally, the M spectra are summed to obtain the spectral components Q of the phased array at range gate g:

$$Q_g(f_i) = \sum_{m=1}^{M} P_{mg}(f_i)S_{mg}(f_i). \tag{13}$$

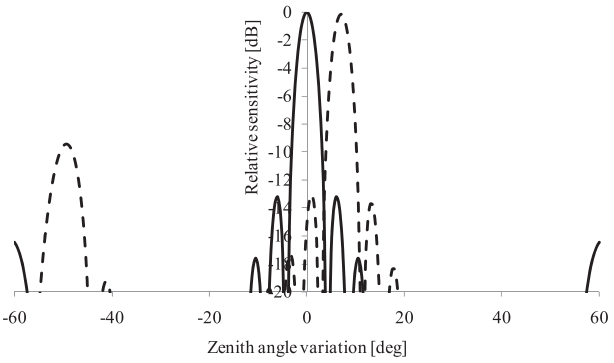

FIG. 10. Array sensitivity (dB) for no phase shift (solid line) and 30° shift in pointing angle (dashed line).

This spectrum is analyzed to find the frequency $f_T + \Delta f_g$ of the spectral peak, and hence to calculate $\mu_g = -c\Delta f_g / f_T$.

f. Beam sensitivity

The overall amplitude response of the phased array is

$$G\frac{\sin\left\{\frac{M}{2}kd[\sin(\beta - \beta_0) - \sin(\beta_g - \beta_0)]\right\}}{\sin\left\{\frac{1}{2}kd[\sin(\beta - \beta_0) - \sin(\beta_g - \beta_0)]\right\}}, \quad (14)$$

where G is the angular sensitivity of an individual microphone at an off-axis angle of $\beta - \beta_0$. For the prototype we used Motorola KSN1005A tweeters as microphones, which have an intensity pattern that can be approximated by $\cos^5(\beta - \beta_0)$. The array intensity sensitivity pattern is shown in Fig. 10. There are in general two main interference peaks, but the unwanted one of these is pointed well away from the position of the scattered sound, at the time the array is staring at the sensing volume. The −3-dB beamwidth is ±2°.

The transmitter dish antenna and horn sensitivity have been measured at 3500 Hz (Mikkelsen et al. 2007) with a −3-dB beamwidth of ±3°. At 4500 Hz the beamwidth would be expected to be about ±2°. In the horizontal plane the beamwidth is ±8°, giving reasonable latitude in pointing toward the column being sensed.

3. Hardware design

The prototype bistatic system comprises a horn and parabolic dish reflector transmitter, and two identical phased array receivers. This configuration of a single transmitter that transmits sound vertically and multiple inclined phased array receivers is chosen because other configurations, such as a single vertically pointing receiver and multiple inclined transmitters, require more power and the use of multiple transmit frequencies.

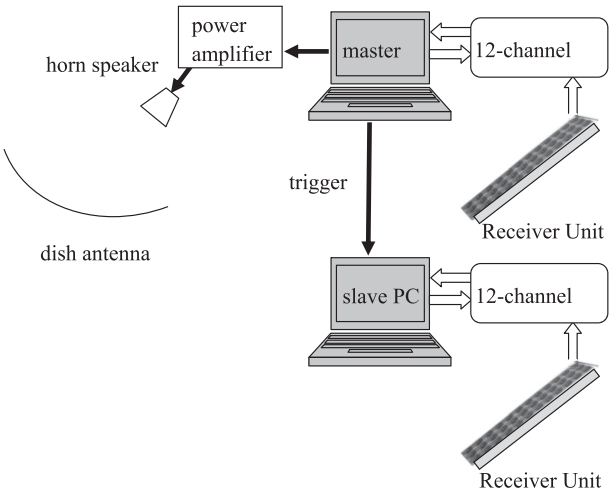

FIG. 11. The hardware system for the prototype bistatic sodar.

A master PC generates the transmitted signal, which is sent to the horn through a power amplifier. The master PC receives signals from one of the phased array receivers (unit 1) and also generates a trigger signal that is sent to a slave PC. The slave PC controls sampling from a second phased array receiver (unit 2). All timing is therefore controlled by the master PC.

Each receiver array consists of 12 rows, each containing three microphones (actually KSN1005A superhorn tweeters used as microphones). The voltage outputs from each group of three microphones are summed. This has the effect of confining the lateral (azimuth) receiver sensitivity, while also cancelling some of the random noise. Each of the 12 grouped outputs is amplified, using a low-noise preamplifier, and bandpass filtered. Digitization is achieved using a Data Translation DT9836 usb module, which can sample the 12 channels simultaneously at up to 225 kHz (see Fig. 11). The dish antenna and each receiver are mounted on a stand with an adjustable zenith angle (see Fig. 12).

4. Field test

A short field test was conducted to check the basic amplitude and Doppler behavior described above.

a. Scanning bistatic sodar C_T^2 and C_V^2 profiles

The prototype bistatic system was set up at the Risø test facility in Høvsøre, Denmark, with a single transmitter and two phased array receivers. The receivers were each 38 m from the transmitter, with the transmitter–receiver lines at right angles. Receiver unit 1 had hay bales on three sides as an acoustic shield. Unit 2 and the transmitter had no shielding.

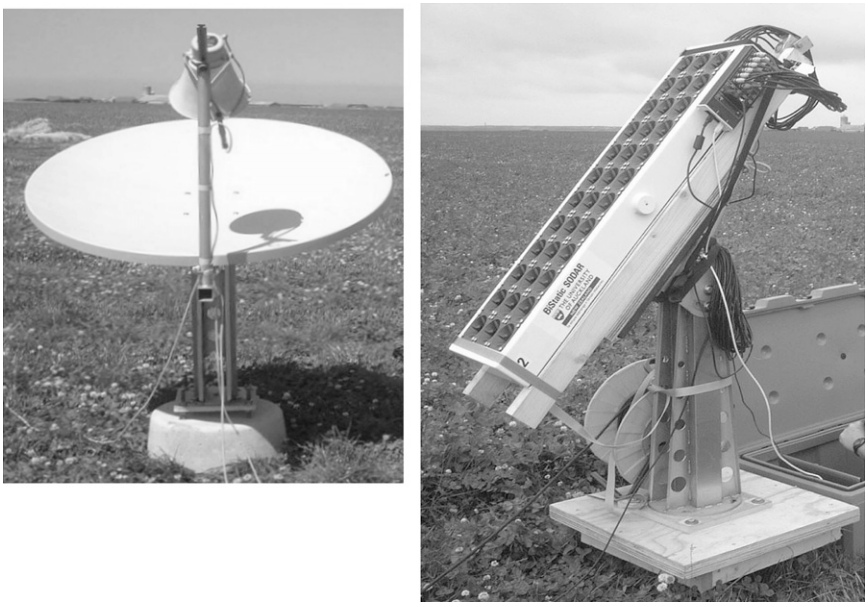

FIG. 12. The dish antenna transmitter and one of the phased array receivers.

The variation of scattered amplitude with height is shown in Fig. 13, using continuous transmission so that the beam steering selectivity could also be tested. Consequently, the large-amplitude lobe near the ground comes from the direct signal but gives an indication that the angular selectivity of the scanning receiver has a half-width of 10 m at the ground, or 15°. However, this apparent beamwidth is mostly due to the pulse length being equivalent to 8.5 m. The expected profile is also shown based on Eqs. (6) and (14) and assuming that $T^2C_V^2c^{-2}C_T^{-2}$ has a constant value of 50 [see Moulsley et al. (1981) for typical measured values of C_V^2 and C_T^2]. The unknown overall antenna gain for the expected profile is arbitrarily chosen, but this does not affect the profile shape. In practice the profile results from a convolution, with the sharp nulls in the beam pattern smoothed out.

The measured profile closely matches that expected, allowing some confidence in being able to retrieve individual C_T^2 and C_V^2 profiles. To do this, receiver unit 1 was placed near the transmitter, facing upward. Because $\beta_1 = 90°$, only C_T^2 is recorded by unit 1. Unit 2, still at 38 m from the receiver and scanning, recorded a combination of the two structure function parameters. The receiver antennas, while identical, are not calibrated absolutely, but from Eq. (6)

$$\frac{P_2}{P_1} = 2^{23/6}\frac{\sin^4\beta}{(1+\sin\beta)^{23/6}}e^{-\alpha D(1-\sin\beta)/\cos\beta}\left[1 + 3.66(1-\sin\beta)\frac{T^2}{c^2}\frac{C_V^2}{C_T^2}\right], \tag{15}$$

allowing the ratio C_V^2/C_T^2 to be estimated as a function of height $z = D\tan\beta$. Since this experiment does not relate directly to precise wind profiling in complex terrain, the results will be reported elsewhere.

b. Scanning bistatic sodar velocity profiles

A comparison was available against mast instruments at 44, 60, and 77 m. Figure 14 shows the mast instrument wind speed record for a 3-h time frame including a period during which bistatic recordings were being made. Figure 15 shows the wind speed profile averaged over six 1-s soundings starting at 1410 LT. For this short run, the error bars are quite large, partly because each spectrum has 1024 points from signals sampled at 12 kHz, which gives 85 ms for the duration of each spectrum and frequency intervals of 12 Hz, equivalent to a velocity interval of nearly 3 m s^{-1}. An improved velocity resolution and smaller error bars are obtained by averaging over many more samples.

5. Conclusions

We have described the design and brief field tests of the first scanned bistatic sodar. This new technology

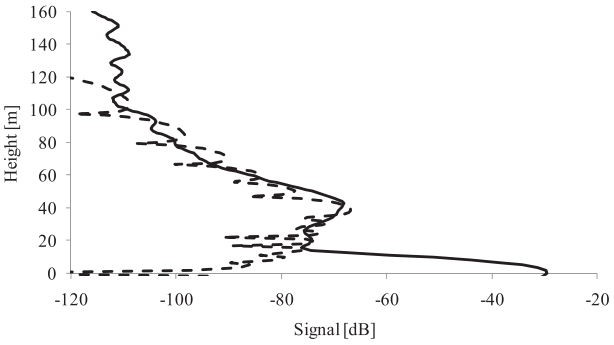

FIG. 13. The variation of received signal amplitude with height. Measurements (solid line) and modeled (dashed line).

potentially has significant advantages over previous bistatic sodars, all of which used a staring mode in which wind data could only be obtained from a confined height range. The main motivation for designing a scanning bistatic sodar, described in the first section, is to avoid errors arising in all current sodars and lidars when they sample nonhorizontally uniform winds. This situation arises generically in complex terrain and, without a solution such as the new bistatic sodar, wind estimates in such regions are considerably compromised.

The result is single-column or mastlike sampling of the wind profile. But there are other advantages that we have identified. These include

- improved signal-to-noise ratio because of the extra scattering from velocity fluctuations;
- much improved performance in neutral lapse conditions, where the turbulent temperature fluctuation contrast is low;
- improved rejection of rain echoes through an advantageous scattering pattern; and
- a larger Doppler shift, reducing the possibility of erroneous velocity estimates arising from echoes from fixed structures.

We describe the relevant theory for each of these factors and how to design a scanning sodar that has good spatial resolution. In particular, it is important to use a pulsed system to avoid the multiple overlapping spectra experienced by the Heimdall sodar (Mikkelsen et al. 2007). In fact, the pulse length largely determines the vertical resolution in the scanned bistatic system. The spectral processing needs to be done rather carefully and certainly is rather more complicated than for a monostatic system. Nevertheless, we found that all spectral processing, and postsampling beam steering, can readily be completed in MATLAB in a small fraction of the profiling time and effectively gives real-time performances.

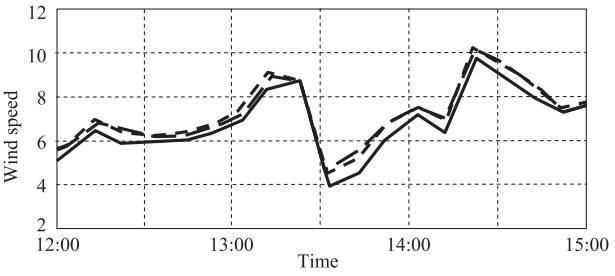

FIG. 14. Wind speed recorded on mast instruments at 44 m (solid line), 60 m (short dashes), and 77 m (long dashes).

A prototype scanning bistatic sodar was designed using a dish antenna transmitter and 12 × 3 arrays of microphones for the receivers. The baseline used in our experiments was 38 m, but this is somewhat arbitrary and there should be further exploration of the optimum configuration. No acoustic baffles (except for the crude use of some hay bales) were used in our prototype. We would expect significant improvements in performance if properly designed acoustic shielding was used.

Very preliminary experiments are described. The profile of the turbulent scattering intensity is found to closely approximate what we expect from theory, giving some confidence in the instrument design and scanning. Comparisons were performed against mast-mounted instruments, and the velocity profile obtained with the bistatic sodar agreed with the ''standard'' instruments to within measurement uncertainties.

We are now progressing to designing microphone-based arrays as an optional addition to a monostatic sodar. This configuration will allow both monostatic and bistatic configuration to operate simultaneously, or sequentially, thereby providing considerable self-checking of the instrument, since the two velocity estimation schemes are quite different.

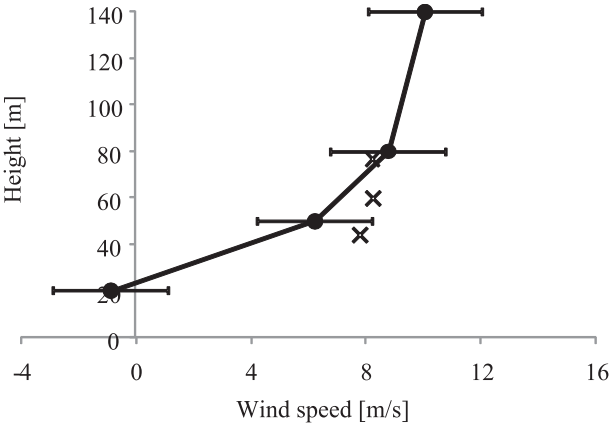

FIG. 15. Wind speeds from the bistatic sodar (solid line and dots) compared with wind speeds from mast instruments (crosses).

Acknowledgments. This work was supported by funding from the European Commission under WP6 of Project Upwind. The authors are grateful for help from the staff of Risø DTU, and in particular, Mike Courtney and the Høvsøre field team led by Bjarne.

REFERENCES

Behrens, P., J. O'Sullivan, R. Archer, and S. Bradley, 2012: Underestimation of monostatic sodar measurements in complex terrain. *Bound.-Layer Meteor.,* **143,** 97–106.

Bingol, F., J. Mann, and D. Foussekis, 2009: Conically scanning lidar error in complex terrain. *Meteor. Z.,* **18,** 189–195.

Bradley, S. G., 2007: *Atmospheric Acoustic Remote Sensing*. CRC Press, 328 pp.

——, 2008: Wind speed errors for LIDARs and SODARs in complex terrain. *Institute of Physics Conference Series, 1, (012061),* 1–7. [Available online at http://www.iop.org/EJ/.]

——, and T. Webb, 2002: Use of an ultrasonic sodar to sense raindrop size distributions. *J. Atmos. Oceanic Technol.,* **19,** 1203–1207.

——, Y. Perrott, P. Behrens, and A. Oldroyd, 2012: Corrections for wind-speed errors from sodar and lidar in complex terrain. *Bound.-Layer Meteor.,* **143,** 37–48.

Coulter, R. L., and K. H. Underwood, 1980: Some turbulence and diffusion parameter estimates within cooling tower plumes derived from sodar data. *J. Appl. Meteor.,* **19,** 1395–1404.

Emeis, S., 2010: *Surface-Based Remote Sensing of the Atmospheric Boundary Layer*. Springer-Verlag, 174 pp.

Mastrantonio, G., G. Fiocco, and A. Marzorati, 1986: Simultaneous operation of a sodar system in monostatic and bistatic modes: Preliminary results. *Atmos. Res.,* **20,** 213–223.

Mathews, T., D. A. Bohlender, and D. Smith, 1986: Effect of refraction of sound on bistatic Doppler sodar measurements of wind profiles. *Atmos. Res.,* **20,** 141–149.

Mikkelsen, T., H. E. Jørgensen, and L. Kristensen, 2007: The bistatic sodar ''Heimdall'': You blow, I listen. Rep. Risø-R-1424(EN), Risø National Laboratory DTU, 32 pp.

Moulsley, T. J., and R. S. Cole, 1993: A general radar equation for the bistatic acoustic sounder. *Bound.-Layer Meteor.,* **19,** 359–372.

——, D. N. Asimakopoulos, R. S. Cole, B. A. Crease, and S. J. Caughey, 1981: Measurement of boundary layer structure parameter profile by using acoustic sounding and comparison with direct measurements. *Quart. J. Roy. Meteor. Soc.,* **107,** 203–230.

Shamanaev, S. V., 2003: Acoustic sounding of raindrop size distribution. *J. Atmos. Oceanic Technol.,* **20,** 152–158.

Thomson, D. W., and R. L. Coulter, 1974: Analysis and simulation of phase coherent acdar sounding measurements. *J. Geophys. Res.,* **79,** 5541–5549.

Underwood, K. H., 1981: Sodar signal processing methods and the Risø-78 experiment. Ph.D. dissertation, The Pennsylvania State University, 178 pp.

Wesely, M. L., 1976: The combined effect of temperature and humidity fluctuations on refractive index. *J. Appl. Meteor.,* **15,** 43–49.

Zinichev, V. A., N. A. Mityakov, V. O. Rapoport, and Yu. A. Sazonov, 1997: Bistatic sodar based on 15-meter overall review radiotelescopes. *Radiophys. Quantum Electron.,* **40,** 877–878.